Time-dependent plasma transport simulation for the study of edge impurity radiation dynamics with magnetic island in large helical device

Time-dependent plasma transport simulation for study of edge impurity radiation dynamics with magnetic island in LHD

Masahiro Kobayashi*[1,2] | Mikhail Z. Tokar[1,3]

[1]National Institute for Fusion Science, National Institutes of Natural Sciences, 322-6 Oroshi-cho, Toki-city, Japan

[2]Department of Fusion Science, SOKENDAI, 322-6 Oroshi-cho, Toki-city, Japan

[3]Plasma Physics, Research Centre Jülich, Jülich, Germany

Correspondence

*Corresponding author name, Email: kobayashi.masahiro@nifs.ac.jp

The dynamics of impurity radiation distribution during detachment transition with edge magnetic island induced by RMP application are studied numerically by solving time-dependent plasma fluid equations together with impurity and neutral transports in a 2D grid system. Computations provide the appearance of a macroscopic structure in the heat transfer along island separatrix and outside of the island. The resultant parallel temperature gradient generates the plasma flow and the density gradient according to the parallel momentum balance. The resulting plasma flow effectively transports impurity toward X-point region. As a result, the impurity radiation is more intensive near the X-point than in the vicinity of the O-point. This leads to the predominant cooling of the region around the X-point. The results are in agreement with experimental observation with RMP application in LHD. The time scale of the thermal condensation instability is found to be of the order of 10 ms.

KEYWORDS:

Detachment, Impurity radiation, Magnetic island, Resonant Magnetic Perturbation, Helical devices

1 | INTRODUCTION

Divertor heat load mitigation is one of the most crucial issues for realizing nuclear fusion reactors. For this purpose, development of stable divertor detachment operation scenario is very important. In helical devices, it has been observed that the edge magnetic field structure plays a key role in the detachment control. In LHD, it has been found that the application of resonant magnetic perturbation (RMP) field provides stable sustainment of divertor detachment [1,2]. In W7-AS, the size of the edge magnetic island is found to be a key parameter to stabilize detachment [3]. The recent experiments of W7-X with island divertor configuration have also realized a stable operation of complete detachment [4]. The mechanisms of the detachment stabilization have been discussed, such as core-edge coupling through neutral penetration [3], or competition between impurity confinement time and radiation penetration time [5], etc. However, the analyses have been limited to rather simplified models so far, while in order to understand the stability of the detachment, time-dependent analysis with appropriate geometrical effects is essential.

In these contexts, analyses with time-dependent transport simulation with edge magnetic island structure have been prompted, in particular, geometrical effects of the magnetic field structure on the impurity radiation distribution and its consequences for the detachment stabilization have been investigated. The rest of this paper is structured as follows. In the next section, the transport model, geometry, and computation scheme are described. In section 3, the results of the computation are presented, where it is shown that dynamics of radiation layer formation is strongly affected by the magnetic island. The paper is summarized in section 4.
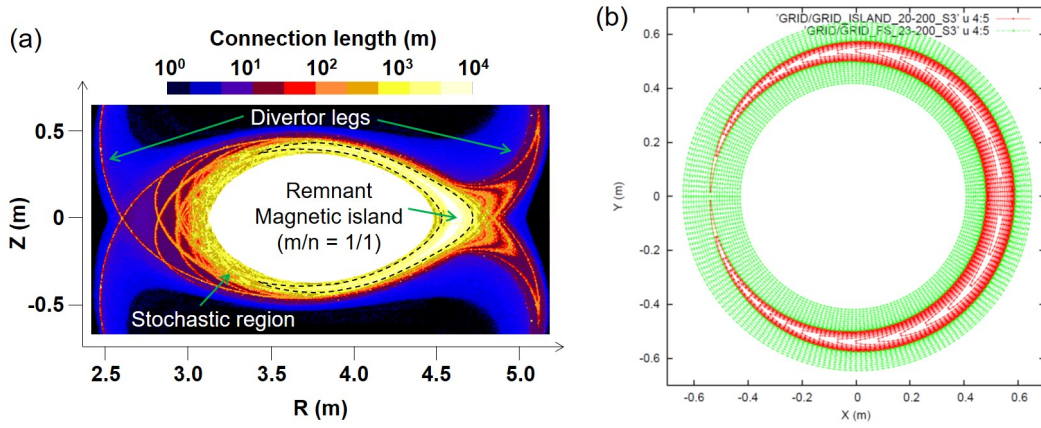
FIGURE 1 (a) Magnetic field line connection length (L_C) distribution with m/n=1/1 magnetic perturbation field in LHD, and (b) the 2D computation grid with magnetic island of m/n = 1/1, which is colored red. The reasoning of the simplification of the magnetic field geometry is explained in section 2. The island is discretized with 20 grid surfaces. The "normal" flux surfaces outside of the island, colored green, are discretized with 12 (radially inner than the island) and 11 (radially outer than the island) grid surfaces, respectively. The poloidal direction is discretized with 200 grid surfaces. Change of magnetic field line lengths (pitch) between the grid points in poloidal direction, which change according to the iota profile, and by singularity around X and O-points, are stored in the grid points.

2 | TRANSPORT MODEL

Figure 1 (a) shows the edge magnetic field structure of LHD with RMP application, which induces edge magnetic island as shown in the figure. Due to the inherent stochasticity at the edge region, the separatrix of the island is no longer clear, but the structure is visible with the bundle of the long flux tubes indicated with the dashed lines. In order to obtain basic physics insight into the geometrical effects of the magnetic island on the impurity radiation dynamics, as a first step, we intend to utilize the simple magnetic field structure in the present analysis. For this purpose, a two dimensional (2D) computation grid is constructed as shown in Fig.1 (b), where the island structure is modeled in a cylindrical geometry.

An RMP field of m/n=1/1 with $\frac{B_r}{B_\phi} = 10^{-3}$ is applied, which induces an edge magnetic island of $\sim 11 cm$ width according to the island width formula, $4 \left(\frac{R_0 B_r}{m |\iota'| B_\phi} \right)^{1/2}$, where $R_0 = 3.90 \, (m)$, $m = 1$, $\iota' = \frac{d\iota}{dr} \approx 5.1 \, (1/m)$, respectively ($\iota = 1/q$). The island structure, which rotates in poloidal direction (θ) as moving in toroidal direction (ϕ), is mapped back to $\phi = 0$ plane to create the 2D grid.

The grid of the magnetic island is colored red, where the island is resolved with 20 radial grid surfaces. The "normal" flux surfaces outside of the island, which are colored green, are discretized with 23 grid surfaces in total, 12 and 11 surfaces at radially inner and outer than the island, respectively. The poloidal direction is discretized by 200 grid points. The magnetic field line lengths (pitch) between the poloidal grid points changes according to the iota profile. Especially, the change is significant near the X and O-points due to the singularity. These changes are stored in the grid points, and used for parallel transport.

In the present model, the divertor legs are degenerated to a boundary condition at the outer-most surface, where Bohm boundary condition is applied as described later in this section. This assumption is introduced accounting for the experimental observations of the low density at the divertor legs, $\sim 10^{18} m^{-3}$ [6,7], which is smaller by an order of magnitude than the density at the stochastic layer, $\geq 1 \times 10^{19} m^{-3}$. Thus impurity radiation is usually larger in the stochastic layer than in the divertor legs as analyzed in ref. [5,8]. The effects of the stochastic layer are not included in the present simplified geometry, but rather we focus on the effects of island structure as mentioned above. The effects of the stochasticity will be addressed in future works with such as enhanced cross-field transport coefficients etc.

The following time-dependent equations for particle, parallel momentum, and energy transport, are solved in the code:

$$\frac{\partial n_i}{\partial t} = \nabla \cdot \left(-n_i V_{i\parallel} \mathbf{b} + D_\perp \mathbf{b}_\perp \mathbf{b}_\perp \cdot \nabla n_i \right) + S_p, \tag{1}$$

$$\frac{\partial m_i n_i V_{i\parallel}}{\partial t} = -\mathbf{b} \cdot \nabla \left(n_i(T_e + T_i) \right) + \nabla \cdot \left(m_i V_{i\parallel} D_\perp \mathbf{b}_\perp \mathbf{b}_\perp \cdot \nabla n_i + \eta_\perp \mathbf{b}_\perp \mathbf{b}_\perp \cdot \nabla V_{i\parallel} \right) - S_m, \tag{2}$$

$$\frac{\partial n_e T_e}{\partial t} = \nabla \cdot \left(\kappa_e \mathbf{b}\mathbf{b} \cdot \nabla T_e + n_e \chi_{\perp e} \mathbf{b}_\perp \mathbf{b}_\perp \cdot \nabla T_e \right) - n_e n_{imp} L(T_e) - S_e - K(T_e - T_i), \tag{3}$$

$$\frac{\partial n_i T_i}{\partial t} = \nabla \cdot \left(\kappa_i \mathbf{b}\mathbf{b} \cdot \nabla T_i + n_i \chi_{\perp i} \mathbf{b}_\perp \mathbf{b}_\perp \cdot \nabla T_i \right) - S_i + K(T_e - T_i), \tag{4}$$

where $\mathbf{b}$ and $\mathbf{b}_\perp$ are local unit vectors parallel and perpendicular to the magnetic field line, respectively. n_e, n_i, $D_\perp$ and $\chi_{\perp e,i}$ are electron and ion densities, particle and heat diffusivities perpendicular to the field lines. $\eta_\perp = m_i n_i D_\perp$ $(kg/m/s)$, is a perpendicular viscosity. $\kappa_{e,i} = \kappa_{e0,i0} T_{e,i}^{2.5}$ $(1/m/s)$ is parallel heat conductivities for electron and ion, with $\kappa_{e0,i0} = 2.1 \times 10^{22}, 6.5 \times 10^{20}$, respectively for $T_{e,i}$ in eV. S_p, S_m, $S_{e,i}$ are the source terms for particle, parallel momentum, and energy transport, which are defined as,

$$S_p = k_{ion} n_e (n_{at} + n_{CX}), \tag{5}$$

$$S_m = k_{CX} n_{at} n_i V_{i\parallel}, \tag{6}$$

$$S_e = k_{ion} n_e (n_{at} + n_{CX}) E_{ion+exc} \quad (E_{ion+exc} = 31 eV), \tag{7}$$

$$S_i = -k_{CX} n_i n_{at} (T_{at} - 1.5 T_i). \tag{8}$$

Here k_{ion} and k_{CX} are ionization and charge exchange (CX) rate coefficients (m^3/s). K represents an equilibration coefficient for energy exchange between electrons and ions, $K = \frac{3 m_e n_e}{m_i \tau_{ei}}$ with $\tau_{ei} = 2.03 \times 10^{10} T_e^{1.5}/n_e$ (sec, T_e in eV). The term, $n_e n_{imp} L(T_e)$, is cooling of electron due to impurity radiation, where n_{imp} is an impurity density summed over all charge states, $n_{imp} = \sum_z n_{imp}^{(z+)}$, and $L(T_e)$ $(m^3 W)$ is a cooling rate of the impurity. In the present computations carbon is used as an impurity, of which the divertor plates is made and is dominant radiator in LHD, and non-coronal model with $n_e \tau = 10^{17}$ (sm^{-3}) is used for $L(T_e)$.[9]

The neutrals are introduced as a "cold" atoms at the outer most surface of computation domain, $n_{at}(a)$, and decays in radial direction according to,

$$n_{at}(r) = n_{at}(a) \exp\left(-\int_r^a \frac{k_{ion} + k_{cx}}{V_{at}} n_e(r) \, dr \right), \tag{9}$$

with $V_{at} = \sqrt{\frac{2 T_{at}}{3 m_{at}}}$ and $T_{at} = 3$ eV, assuming Flanck-Condon atoms dissociated from molecules. The collision between the atoms and ions produces "hot" CX neutrals, n_{CX}, transport of which is modeled with fluid approximation as follows,

$$0 = \nabla \cdot \left(D_{CX} \mathbf{b}_\perp \mathbf{b}_\perp \cdot \nabla n_{CX} \right) + k_{CX} n_i n_{at} - k_{ion} n_e n_{CX} \tag{10}$$

$$D_{CX} = \frac{V_i^2}{n_i(k_{ion} + k_{CX})}, \tag{11}$$

with $V_i = \sqrt{\frac{T_i}{m_i}}$. In the present analyses, quasi-neutrality, $n_e \approx n_i$ is assumed. As we checked the ratio n_{imp}/n_e a posteriori in the results of computations, it is a few percent at maximum. So that the present approximation is considered to be valid within the error in this range.

For impurity, by summing up for all charge states, the particle transport equations is reduced to,

$$\frac{\partial n_{imp}}{\partial t} = \nabla \cdot \left(-n_{imp} V_{imp\parallel} \mathbf{b} + D_\perp^{imp} \mathbf{b}_\perp \mathbf{b}_\perp \cdot \nabla n_{imp} \right) + S_p^{imp}, \tag{12}$$

where S_p^{imp} is an ionization rate of neutral impurity to the first charge state, $n_{imp}^{(1+)}$.

The impurity density is initially set zero everywhere at a lowest plasma density computation, where the impurity radiation is reasonably small. Then the neutral impurity flux, $\Gamma_{imp}^{(0)}(a)$, is launched at the outer-most surface proportional to the divertor

TABLE 1 Input parameters for present computations.

$D_\perp$ (m^2/s)	$\chi_{\perp,e,i}$ (m^2/s)	$D_\perp^{imp}$ (m^2/s)	P_{SOL} (MW)	$\frac{B_r}{B_\phi}$	C_{sput}	γ_e	γ_i
1.0	1.0	1.0	8.0	10^{-3}	0.01	5.5	2.0

particle flux, Γ_p, with multiplication factor, sputtering coefficient, C_{sput}, such that $\Gamma_{imp}^{(0)}(a) = C_{sput}\Gamma_p$. The impurity flux then decays radially as,

$$\Gamma_{imp}^{(0)}(r) = \Gamma_{imp}^{(0)}(a) \exp\left(-\int_r^a \frac{k_{ion}^{imp(0)}}{V_{imp}^{(0)}} n_e(r)\, dr\right), \tag{13}$$

where $k_{ion}^{imp(0)}$ is an ionization rate coefficient of neutral impurity, and $V_{imp}^{(0)} = \sqrt{\frac{T_{imp}^{(0)}}{m_{imp}}}$ with $T_{imp}^{(0)} = 2$ eV is assumed. The obtained n_{imp} distribution is used as a initial condition for the next computations with increased plasma density ($n_{at}(a)$).

The parallel impurity velocity, $V_{imp\parallel}$, is obtained by assuming force balance between the friction force and the ion thermal force (ion temperature gradient force) [10],

$$V_{imp\parallel} = V_{i\parallel} + \frac{\tau_s C_i}{m_{imp}} \mathbf{b} \cdot \nabla T_i, \tag{14}$$

with $C_i = 2.6 Z_{imp}^2$ and $\tau_s = 2.05 \times 10^{13} \frac{m_{imp}}{\ln\Lambda\, n_i Z_i^2 Z_{imp}^2 \sqrt{m_i}} \frac{T_i^{1.5}}{\frac{m_i}{m_{imp}}+1}$, $(\ln\Lambda = 17)$, the impurity slowing down time. It is noted that the above equation becomes charge independent due to the cancellation of Z_{imp} between C_i and τ_s. $D_\perp^{imp} = D_\perp$ is assumed for the present computations. Carbon, sputtered from the divertor target plates, is considered as the dominant impurity species

The boundary conditions are defined as follows. At the inner-most surface, power flux to the computation domain, P_{SOL}, is given, which is uniformly distributed in a poloidal direction, and is equally divided to electrons and ions. The neutral flux that penetrates into the confinement region through the inner-most surface is given to plasma particle as a net flux through the boundary. As mentioned above, the divertor legs are degenerated to a boundary condition at the outer-most surface, where Bohm boundary condition is applied for particle and energy transport with multiplication factor β, that is, $\Gamma_p = \beta n c_s$ and $\Gamma_e = \beta(\gamma_e T_e + \gamma_i T_i) n c_s$, with $c_s = \sqrt{\frac{T_e + T_i}{m_i}}$, sound speed, and $\gamma_{e,i}$ being sheath heat transmission coefficients for electron and ion, respectively. Here $\beta = \mathbf{r} \cdot \mathbf{b} = \frac{B_r}{B_\phi} \approx 10^{-3}$ is introduced to convert the particle and energy flux at the divertor plates to the perpendicular flux at the outer-most surface.

The input parameters used in the present computations are summarized in table 1 . The transport equations are integrated by applying an implicit finite volume scheme on the 2D grid. The time step of the computations are set to $2 \times 10^{-7} \sim 2 \times 10^{-8}$ (sec). The atom density at the outer-most surface, $n_{at}(a)$, is gradually increased to reproduce a prescribed level of the electron density at the core boundary, and thus to induce detachment transition. This method mimics gas puff scan in experiments.

3 | RESULTS OF COMPUTATIONS

The computations are started with low plasma density where the impurity radiation is reasonably small, and density is gradually increased by increasing $n_{at}(a)$ stepwise. Usually, the computation reaches steady state within physical time of 0.1 - 0.2 sec after the stepwise increase of $n_{at}(a)$. When $n_{at}(a)$ was increased to $2.9 \times 10^{17} m^{-3}$, the radiated power from the impurity starts to exceed the power to the divertor plates. At the convergence, the power balance with respect to P_{SOL} is as follows. The power to the divertor plates: 25%, the power of impurity radiation: 54%, energy loss via hydrogen (excitation and ionization): 11%, energy loss via CX: 10%. When $n_{at}(a)$ was increased to $3.0 \times 10^{17} m^{-3}$, rapid increase of radiated power and concomitant decrease of the divertor power/particle load are encountered after 47 millisecond in physical time.

The time traces of radiated power and divertor particle flux integrated over the computation domain are plotted in Fig. 2 (a). The onset of detachment transition, t = 0 sec, is defined at the timing of decrease of the divertor particle flux as shown in Fig. 2 (a). It is seen that the radiated power fraction starts increasing significantly after the onset, even slightly exceeding 100%, during
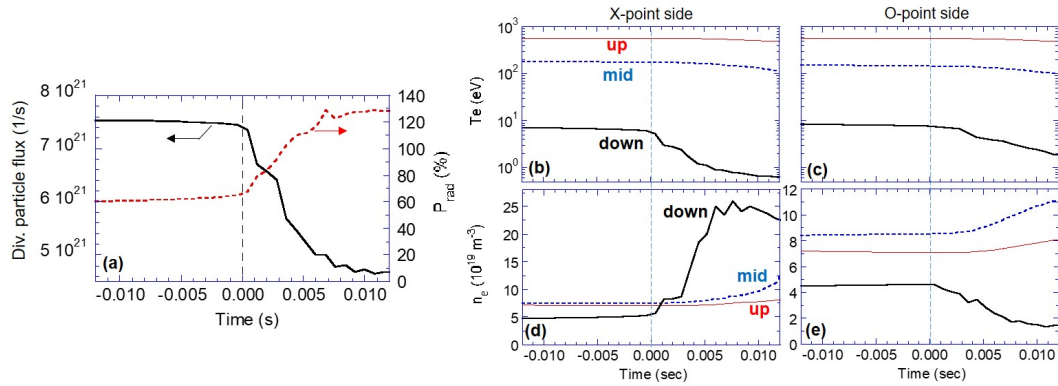
FIGURE 2 Temporal evolution of (a) divertor particle flux and radiated power, (b, c) T_e, and (d, e) n_e at different locations during detachment transition. The onset of detachment, t = 0 sec, is defined as the start of the divertor particle flux decrease. "up" and "down" indicate innermost and outermost radial surfaces, and "mid" is the middle point between them, at Y = 0 m plane in Fig.1 (b), respectively. X- and O- points sides mean the region of X < 0 and X > 0 m in Fig.1 (b), respectively.

which significant cooling of plasma takes place in an unsteady state. The temporal evolution of T_e and n_e at various locations are also plotted in Figs. 2 (b-e). T_e at the downstream (outermost radial surface) of X-point region (Fig. 2 (b), "down") starts to decrease at the same time of the divertor particle flux reduction. On the other hand, T_e at at the downstream of O-point region (Fig. 2 (c), "down") decreases with delay. This indicates that the detachment is initiated around the X-point. n_e at the downstream of X-point region (Fig. 2 (d), "down") shows significant increase right after the detachment onset. This is due to the thermal condensation instability caused by the magnetic field structure of the island as explained below.

Figure 3 shows 2D distribution of plasma parameters during the detachment transition. From Fig.3 (a1-3), it is observed that the radiated power by impurity, P_{rad}, is enhanced around/at the X-point. This is found to be due to the geometrical effect of the island structure on the transport, as explained in the following.

Along the island separatrix, which connects radially inner and outer regions of O-point, parallel temperature gradient is developed through parallel transport, as indicated by arrows in Fig.3 (b1), where the arrow directions indicate the direction of energy flux. The energy flux that reaches the outer edge of the O-point diffuses out perpendicularly and, at the same time, transported toward the side of X-point through parallel transport, as indicated by the outer-most arrows in Fig.3 (b1), and thus develops parallel temperature gradient there. Through the parallel momentum balance, these temperature gradients develop parallel flow, $V_{i\parallel}$, in the same direction of the arrows in Fig.3 (b1). The impurity flow, $V_{imp\parallel}$, was found to have similar flow pattern as $V_{i\parallel}$. The resulting flow field of $V_{imp\parallel}$ is plotted in Fig.3 (d) as a poloidal projection of the parallel flow. The flow at the outer-most region is clearly visible, which is directed toward the side of X-point. This outer-most flow is most effective to drive the impurity toward the side of X-point, since the impurity comes from the outside of plasma and has the largest density at the periphery. Due to the increased impurity at the X-point side, P_{rad} is increased. This geometrical effect is observed already at the attached phase, and is enhanced as approaching the detachment onset since temperature gradient develops further due to the lowering of the temperature.

After the detachment onset, the radiation region moves radially inward as shown in Fig.3 (a2), and the temperature is further cooled down, Fig.3 (b2). The impurity flow towards the X-point side and localization of impurity there are enforced as seen in Figs.3 (d2), and (e2). The density peaking at the radiation region is also observed through the momentum conservation, Fig.3 (c2). These processes facilitate each other, leading to the radiation increase at the X-point region, exhibiting thermal condensation instability. At t = 12 ms, the peaked radiation reaches the X-point. Indication of the X-point radiation is also observed in experiments with AXUV and bolometer measurements[1,11]. The process described above may explain the experimental observation.

The computations were further continued and the radiation layer penetrates further into the island, where the temperature of the island decreases down to ~ 1 eV. In the experiments, on the other hand, the temperature at the island is kept at around 10 to 20 eV and the radiation region seems to stay around the X-point. This discrepancy between the modeling and the experiments will be further studied by investigating various aspects of the model, such as dynamical change of impurity sputtering coefficient
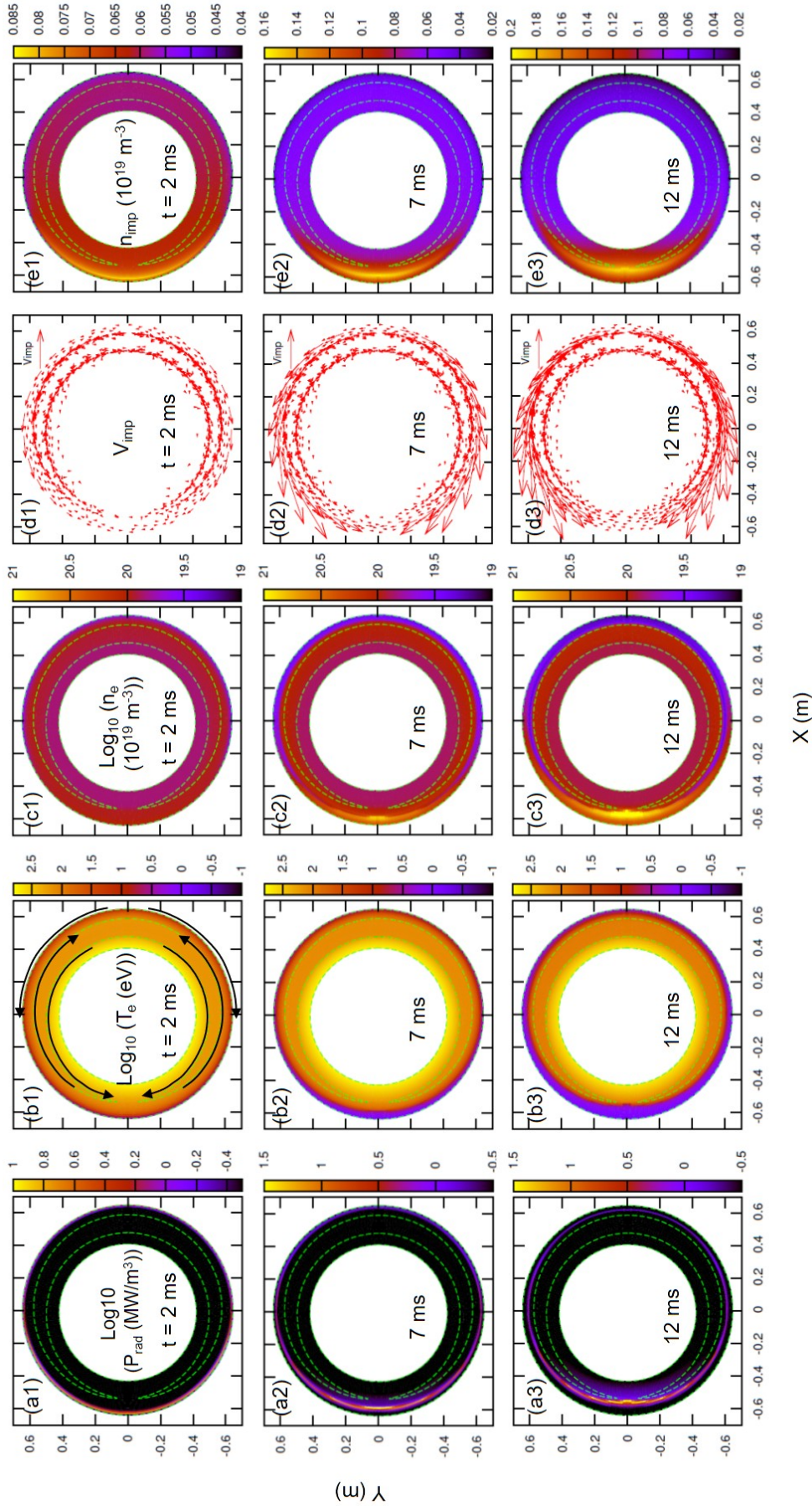
FIGURE 3 2D distributions of (a) impurity radiation P_{rad}, (b) electron temperature T_e, (c) electron density n_e, (d) vector field plot of parallel impurity flow V_{imp} projected in poloidal cross section, and (e) impurity density n_{imp}. The time t = 0 sec is taken at the onset of detachment transition. The arrows in (b) represent direction of energy flux. In the vector plots, length of the arrows of 0.1 m correspond to 10^4 m/s, and linearly scales. The structure of the island is indicated by dashed lines in each panel.

and of perpendicular transport due to detachment transition, and effects of magnetic field stochastization, such as cross-field interaction of parallel flow, etc.

4 | SUMMARY

The effects of edge magnetic island, which is induced by RMP application, on the impurity radiation distribution and on its dynamics during detachment transition have been investigated by solving a set of plasma, impurity, and neutral transport equations with a time-dependent implicit finite volume scheme in a 2D grid system that captures the island geometrical effects. The computations show that the global energy flux and plasma flow structures appear along the island separatrix and outside of the island. The background plasma flow effectively drives the impurity toward the X-point region, and then enhances the impurity radiation there. This effect is more pronounced as the detachment transition proceeds and facilitates the thermal condensation instability at the X-point. The time scale of the instability is an order of 10 ms. The results are in agreement with the experimental observation with radiation measurements. However, the stabilizing effect of the radiation that is observed in experiments has not been reproduced. Further analysis by refining the transport model is foreseen in the near future.

ACKNOWLEDGMENTS

References

[1] M. Kobayashi et al., *Nuclear Fusion* **2013**, *53*, 093032.

[2] M. Kobayashi et al., *Nuclear Fusion* **2019**, *59*, 096009.

[3] Y. Feng et al., *Nuclear Fusion* **2006**, *46*, 807.

[4] P.S. Pedersen et al., *Nuclear Fusion* **2019**, *59*, 096014.

[5] M. Kobayashi, M.Z. Tokar, *Experimental Studies of and Theoretical Models for Detachment in Helical Fusion Devices*, IntechOpen, London, **2019**.

[6] S. Masuzaki et al., *Nuclear Fusion* **2002**, *42*, 750 – 758.

[7] M. Kobayashi et al., *Fusuion Science and Technology* **2010**, *58*, 220 – 231.

[8] T. Kobayashi et al., *Nuclear Materials and Energy* **2019**, *19*, 239.

[9] D.E. Post, *Journal of Nuclear Materials* **1995**, *220-222*, 143 – 157.

[10] P.C. Stangeby, *The Plasma Boundary of Magnetic Fusion Devices*, IOP Publishing, London, **2000**.

[11] S.N. Pandya et al., *Nuclear Fusion* **2016**, *56*, 046002.

☐